

Highly Sensitive, Fast Graphene Photodetector with Responsivity $> 10^6$ A/W Using Floating Quantum Well Gate

Krishna Murali, Nithin Abraham, Sarthak Das, Sangeeth Kallatt, and Kausik
Majumdar*

*Department of Electrical Communication Engineering,
Indian Institute of Science, Bangalore 560012, India*

E-mail: kausikm@iisc.ac.in

Abstract

Graphene, owing to its zero bandgap electronic structure, is promising as an absorption material for ultra-wideband photodetection applications. However, graphene-absorption based detectors inherently suffer from poor responsivity due to weak absorption and fast photocarrier recombination, limiting their viability for low intensity light detection. Here we use a graphene/WS₂/MoS₂ vertical heterojunction to demonstrate a highly sensitive photodetector, where the graphene layer serves dual purpose, namely as the light absorption layer, and also as the carrier conduction channel, thus maintaining the broadband nature of the photodetector. A fraction of the photoelectrons in graphene encounter ultra-fast inter-layer transfer to a floating monolayer MoS₂ quantum well providing strong quantum confined photogating effect. The photodetector shows a responsivity of 4.4×10^6 A/W at 30 fW incident power, outperforming photodetectors reported till date where graphene is used as light absorption material by several orders. In addition, the proposed photodetector exhibits an extremely low noise

equivalent power (NEP) of $< 4 \text{ fW}/\sqrt{\text{Hz}}$ and a fast response (\sim milliseconds) with zero remanent photocurrent. The findings are attractive towards the demonstration of graphene-based highly sensitive, fast, broadband photodetection technology.

Keywords

Graphene, MoS₂, WS₂, Photodetection, Photogating effect, van der Waals heterojunction

1 Introduction

Photodetectors operating in the infra-red spectral regime find widespread applications across different areas, such as military, space, communication, and medical imaging, to name a few.¹⁻⁵ Technologies based on III-V semiconductors,^{6,7} Pb based quantum dots^{8,9} and mercury cadmium telluride^{10,11} currently dominate this space. However, there is a notable research focused on simplifying the fabrication process, reducing material cost, using non-hazardous materials in terms of environment, health and safety, and improving the detector performance at room temperature, thereby eliminating additional cooling requirements.

Graphene can absorb light of extremely wide wavelength range (ultra-violet to terahertz wavelength regime) due to its unique gapless band structure.¹² Graphene is thus widely considered as a promising material for broadband photodetection and hence is attractive for a plethora of applications.¹³⁻¹⁶ Further, the graphene-based photodetectors exhibit ultra-fast operation¹³ due to superior carrier mobility. Unfortunately, graphene photodetectors typically do not show high sensitivity due to two important issues. First, the ultra-thin nature of graphene impedes the overall light absorption efficiency. For example, a monolayer-thick graphene absorbs only about 2.3% of the light intensity incident on it.¹⁷ Second, photo-excited carriers in graphene possess short lifetime which is on the order of picoseconds.^{18,19} One must separate the photo-generated electron-hole pairs within a time scale that is less

than the photocarrier lifetime in order to generate a sizeable photocurrent. Consequently, a majority of the reported photodetectors in literature where graphene is used as light absorption medium, including graphene/metal junction,^{20–22} p-n junction using graphene,^{15,23} and bilayer graphene under an electrical bias,²⁴ exhibit weak sensitivity.

In this context, there has been a considerable amount of effort towards achieving photodetectors with a large responsivity by using photogating effect.^{25–38} However, these structures primarily use graphene as a photocarrier transport layer, while the light absorption occurs in a different material, for example, transition metal dichalcogenides,^{32,39,40} quantum dots^{31,41,42} and perovskites.^{42–44} The corresponding threshold wavelength of the photo-absorbing material thus limits the operation range of the photodetector, and the broadband nature of the photodetection that graphene offers is completely lost. In addition this, these detectors employing photogating while can achieve a high-gain, suffer from slow response, and exhibit a large reminiscent photocurrent^{31,32,39,45,46} due to slow de-trapping of carriers. To mitigate this, it has been proposed in the past to flush the trapped carriers using a gate voltage pulse which can restore the initial state of the device.^{31,32} However, such an arrangement requires additional circuits and thus increases the system level complexity. In order to eliminate these bottlenecks, in this work, we propose and demonstrate a novel photodetector that uses a vertical van der Waals (vdW) heterojunction comprising of graphene/WS₂/MoS₂ stack. In the proposed structure, graphene serves as the light absorbing layer and the carrier transport layer, while the MoS₂ quantum well serves as a floating gate. The device simultaneously achieves ultra-high responsivity, extremely low noise, fast photodetection with no reminiscent photocurrent at room temperature over a broad wavelength range facilitating broadband operation.

2 Results and discussions

2.1 Principle of operation

The architecture and working principle of the proposed device is explained schematically in Fig. 1a-c. The vertical stack consists of a monolayer (1L) or bilayer (2L) WS_2 film sandwiched between few-layer graphene (FLG) on top and 1L- MoS_2 at the bottom. The whole stack is placed on Si substrate coated with 285 nm thermally grown SiO_2 . MoS_2 having a conduction band offset with WS_2 , as shown in Fig. 1c, creates an ultra-thin quantum well for electrons, with SiO_2 on the other side. Under light illumination with photon energy less than the excitonic gap of MoS_2 (and WS_2), electron-hole pairs are generated only in the graphene layer. Since inter-layer carrier transfer process in vdW heterojunction is extremely fast (\sim sub-ps),⁴⁷⁻⁵⁰ a fraction of the photo-generated electrons are transferred to the MoS_2 quantum well through the ultra-thin WS_2 layer before recombination in graphene (Fig. 1b and left panel of Fig. 1c). Depending on the wavelength of excitation, both tunneling and over-the- WS_2 -barrier transfer processes are possible. The electrons, after being transferred to MoS_2 , swiftly thermalize to the conduction band edge of MoS_2 . A fraction of these carriers can also be captured by the sub-bandgap trap states⁵¹ in MoS_2 . The trapped carriers in the MoS_2 quantum well can in further tunnel through the WS_2 barrier layer to come back to graphene. These population and depopulation mechanisms are quite fast due to the ultra-fast nature of the inter-layer charge transfer, which help to quickly create a steady state photoelectron population in the MoS_2 floating quantum well. The WS_2 spacer being an ultra-thin layer allows strong electrostatic coupling between the MoS_2 layer and the graphene channel. The MoS_2 quantum well with the captured photoelectrons thus acts as a floating gate on the graphene channel, modulating the Dirac point and the in-plane conductivity of the FLG film, in turn generating a measurable change in the current as detected by the electrodes shown in Figs. 1a-b.

Note that there is a strong built-in field due to the offset of the conduction band edges between MoS₂ and graphene, as shown in the band diagram in Fig. 1c. Such field favors a fast inter-layer transfer of the stored photoelectrons in MoS₂ to graphene. When the light source is turned off (Fig. 1c, right panel), the captured photoelectrons in the MoS₂ quantum well thus swiftly tunnel through the WS₂ barrier layer to graphene, and thus switching off the gating action immediately. This mechanism allows us to completely suppress the remanent photocurrent. Further, we do not need an external gate pulse to flush the confined photoelectrons. The detector thus is expected to exhibit a fast response due to the intrinsically small time scale of the inter-layer charge transfer and the high in-plane carrier mobility in graphene.

2.2 Evidence of carrier storage in MoS₂ floating quantum well

Fig. 2a shows the optical image of a fabricated FLG/1L-WS₂/1L-MoS₂ stack, along with isolated 1L-WS₂ and 1L-MoS₂ portions as controls. The Raman shifts from the isolated portions, as well as from the junction are shown in Fig. 2b. Under illumination, to demonstrate the charge storage in the bottom monolayer MoS₂ without immediately being transferred to graphene through WS₂, we employ photoluminescence (PL) quenching measurement. Figs. 2c-d show the PL intensity acquired from the isolated 1L-WS₂ (in orange), isolated 1L-MoS₂ (in green) and the junction (in black) separately at 150 K and 295 K with 532 nm laser excitation. At 150 K the monolayer WS₂ shows the exciton (A_{1s}) peak around 2.07 eV and the trion (A_{1s}^T) peak around 2.04 eV, whereas the monolayer MoS₂ exhibits the A_{1s} peak around 1.94 eV, and the A_{1s}^T peak at around 1.90 eV. On the junction, although there is no significant change in the peak position in the PL spectra (due to a combined effect of bandgap renormalization and exciton binding energy reduction^{52,53}), the WS₂ PL shows almost 90% to 95% quenching of the exciton and the trion peaks. This indicates an ultra-fast

inter-layer charge transfer from WS₂ to both graphene and MoS₂ before the radiative decay of the exciton. On the contrary, the MoS₂ peaks do not show any significant quenching in the PL spectra at the junction. At 295 K, the peaks are red shifted due to a reduction in bandgap, but the observations regarding quenching remain similar to that at 150 K.

Further, to avoid any possible compensation effect by photo-carrier injection from WS₂ to MoS₂, we reduce the temperature to 3.7 K, thus pushing up the excitonic gap of 1L-WS₂ to 2.1 eV, and selectively excite only the 1L-MoS₂ layer at the junction with 633 nm laser as the photon energy (~ 1.96 eV) is lower than the 1L-WS₂ optical bandgap. The results as shown in Fig. 2e suggest that PL intensity of the trion peak (the exciton peak being truncated by the edge filter due to resonant excitation) of MoS₂ is similar in isolated portion and at the junction. This unambiguously shows that it is possible to create a steady state population of stored photo-carriers in the MoS₂ quantum well without being immediately transferred to graphene - allowing for the proposed photogating action. To confirm the point further, we also perform circular polarization resolved PL experiment using near resonant excitation in MoS₂ by 633 nm laser at 3.7 K (Fig. 2f). We obtain a similar degree ($\sim 25\%$, obtained by peak fitting with Voigt function) of circular polarization for the trion peak both on the isolated MoS₂ (left panel) and on the junction (right panel), which indicates that the valley polarization of MoS₂ trions remains intact at the junction. This further justifies suppression of additional scattering channel in MoS₂ at the junction owing to desirable carrier confinement. Note that, at low temperature, we observe strong sub-bandgap luminescence both from WS₂ and MoS₂, indicating presence of defect states,^{54–57} which play an important role in obtaining large photodetector gain, as explained later.

2.3 Photodetector fabrication and characterization

The photodetector (D1) fabrication process steps are illustrated in Fig. 3a. The device fabrication process starts with mechanical exfoliation of MoS₂ flakes over Si substrate coated with 285 nm SiO₂. 1L-MoS₂ flakes are identified by optical contrast and Raman spectroscopy. The 2L-WS₂ flake is then transferred on top of the 1L-MoS₂ flake using a micromanipulator under optical microscope. For making MoS₂ island, we use electron beam lithography, followed by dry etch using chlorine chemistry. FLG flake is then transferred on the heterostructure. Electrodes for contacting the FLG film are then defined by a second electron beam lithography step, followed by the deposition of Ni (10nm)/ Au (50nm) electrodes by DC sputtering and subsequent lift-off. A third lithography step followed by a final etch step is used to form a regular pattern of the FLG film so that graphene falls only on top of the WS₂/MoS₂ junction area, avoiding any un-gated parallel conduction path. More details on the layer transfer and device fabrication are provided in the **Methods** section. The junction area of the fabricated device is 6 μm^2 .

To demonstrate the concept proposed, we choose few-layer graphene over monolayer as the active layer. While monolayer graphene exhibits more gate tunability over few-layer, the choice of few-layer is to (1) enhance light absorption, (2) suppress substrate trap induced noise, and (3) reduce ambience induced detrimental effects. We also choose 2L-WS₂ over 1L as the sandwiched barrier layer (1) to improve over-the-barrier injection from graphene to MoS₂ due to suppressed barrier height, and (2) to increase the tunnelling width for band edge electrons in MoS₂ to move back to graphene, thereby increasing the steady state population of captured photoelectron density in MoS₂ floating gate. Fig. 3b shows the PL spectra of 1L-MoS₂/2L-WS₂ stack at 295 K, and the band-offset between the two can be inferred from the different peaks, as illustrated in Fig. 3c. The free exciton peaks of MoS₂ (A and B) and WS₂ (A) are distinctly observed from the isolated portions. The 2L-WS₂ also clearly shows the indirect peak around 1.75 eV, indicating its bilayer nature. At the junction

area, the exciton and indirect peaks of WS_2 are quenched whereas the MoS_2 peaks are distinctly discernable. We also observe a distinct inter-layer exciton peak at 1.45 eV, which is absent in the individual layers, indicating strong electronic coupling between the vdW layers.

The I_d - V_g characteristics of the FLG under dark condition is shown in Fig. 4a, with a Dirac voltage (V_D) around -10.8 V indicating n-type doping. We operate the device as a photodetector keeping the external gate voltage as zero. The operating point under dark condition is indicated by point P_1 . Under illumination, the captured photoelectrons by the MoS_2 quantum well electrostatically gates the FLG, pushing the device operating point towards left to P_2 , providing a negative photocurrent, as schematically depicted in Fig. 1c. The top inset of Fig. 4a shows the drain voltage (V_d) dependent dark current under zero gate bias.

Fig. 4b shows the measured photocurrent ($I_{ph} = I_{light} - I_{dark}$) of the photodetector D1 as a function of V_d , for three different optical powers (P_{op}) incident on the junction, at 532 nm excitation wavelength. Figs. 4c-e show the transient response of the photodetector at 532 nm, 785 nm, and 851 nm, respectively, illustrating fast switching for the incident powers used. The measured rise and fall times are found to be < 10 ms, and only limited by the resolution of the measurement equipment. We do not observe any reminiscent photocurrent in the transient characteristics, which are typically observed in high-gain detectors using photo-gating effect. As mentioned earlier, this is achieved by the inherent built-in field in the device in the vertical direction that swiftly pushes the captured photo-carriers to graphene channel when light is turned off. This eliminates the requirement for additional refreshing circuit to push the detector to its original state. Note that the noise level is higher for the 532 nm excitation, which limits the detection of low power optical signal, while the noise level for 785 nm and 851 nm excitation is much lower, even when the incident power is very low (bottom panels of Figs. 4d-e). 532 nm photons having energy higher than the excitonic bandgap of MoS_2 (and WS_2), can be directly absorbed by these layers. The photo-generated

large hot carrier density in MoS₂ can in turn directly interact with the trap states in SiO₂ substrate, causing a large noise. On the other hand, when excitation energy is smaller than MoS₂ excitonic gap (for example, 785 and 851 nm), only graphene absorbs the excitation, followed by photoelectron transfer to MoS₂ quantum well. During this process, the hot photo-carriers lose their energy, which significantly suppresses the interaction with the substrate traps states, reducing the gain noise and allowing us to detect optical signal down to 30 fW.

Using the above argument, the ultra-low noise level exhibited by the photodetector at sub-bandgap excitation of MoS₂ and WS₂ helps us to rule out a direct absorption by the defect states in these materials. Further, absorption of the near-infrared wavelengths used in this work would require involvement of deep level trap states of MoS₂ and WS₂. De-trapping of photocarriers from such deep trap states would be very slow, and would result in a slow decay of the photocurrent. The fast transient response observed from the detector thus corroborates that the effect of direct sub-bandgap absorption in MoS₂ and WS₂ layers can be ignored in our work.

2.4 Performance evaluation, modeling, and benchmarking

The extracted responsivity ($R = \frac{I_{ph}}{P_{op}}$) of the photodetector is plotted in Fig. 5a as a function of incident optical power density for different wavelengths of excitation at $V_d = 0.5$ V. There are two remarkable observations from this plot. First, the magnitude of the responsivity, particularly at low power density, is extremely high, reaching 4.4×10^6 A/W at the minimum power density applied. This is several orders of magnitude higher than that of any reported detector based on light absorption by graphene, as shown in Table 1. Second, the responsivity follows the same trend line irrespective of the wavelength of the incident light, in agreement with broadband light absorption by graphene.

In order to get insights into such high gain mechanism in the detector, we construct a unified model that captures the density dependent recombination time of photo-carriers in graphene (τ_r),^{19,58} fast inter-layer transfer of photo-carriers from graphene to MoS₂ floating gate (τ_{GM}) and vice versa (τ_{MG}), and possible trapping (τ_{MT}) and de-trapping times (τ_{TM}) of the carriers^{59,60} in the MoS₂ bandgap. The coupled differential equations that govern the photoinduced carrier densities in graphene (Δn_G) and MoS₂ (Δn_M), and the trapped carrier density in MoS₂ (n_T) are given by

$$\frac{d\Delta n_G}{dt} = \eta\phi - \frac{\Delta n_G}{\tau_r(\Delta n_G)} - \frac{\Delta n_G}{\tau_{GM}} + \frac{\Delta n_M}{\tau_{MG}} \quad (1)$$

$$\frac{d\Delta n_M}{dt} = \frac{\Delta n_G}{\tau_{GM}} - \frac{\Delta n_M}{\tau_{MG}} + \frac{n_T}{\tau_{TM}} - \frac{\Delta n_M}{\tau_{MT}} \left(1 - \frac{n_T}{N_T}\right) \quad (2)$$

$$\frac{dn_T}{dt} = \frac{\Delta n_M}{\tau_{MT}} \left(1 - \frac{n_T}{N_T}\right) - \frac{n_T}{\tau_{TM}} \quad (3)$$

where N_T is the trap state density in MoS₂ per unit area, η is internal quantum efficiency of few-layer graphene absorption, and ϕ is the photon flux. Under steady state condition, putting the left hand sides of equations (1)-(3) to zero, and realizing that there is no net flow of charge from graphene to MoS₂, we analytically obtain $\Delta n_G = \eta\phi\tau_r(\Delta n_G)$, $\Delta n_M = \frac{\Delta n_G\tau_{MG}}{\tau_{GM}}$, and $n_T = \frac{\Delta n_M N_T}{\Delta n_M + N_T} \frac{\tau_{MT}}{\tau_{TM}}$. The responsivity can then be calculated as

$$R_{calculated} = \frac{q}{hc} \frac{\lambda g_m (\Delta n_M + n_T)}{A C_{ox} \phi} \quad (4)$$

where h is Plank constant, q is absolute electron charge, c is velocity of light, λ is the excitation wavelength, g_m is the extracted transconductance from Fig. 4a at operating point P_1 , A is device active area, and C_{ox} is back gate oxide capacitance. The orange curve is the simulated responsivity with fitting parameters $\frac{\tau_{MG}}{\tau_{GM}} = 10$, $\frac{\tau_{MT}}{\tau_{TM}} = 5 \times 10^{-4}$, and $N_T = 5 \times 10^{10}$ cm⁻². In the same plot, we also show the calculated R by turning off the trap states in the model, as denoted by the blue curve. At high incident optical power density, the traps in MoS₂ play a less important role and photocurrent saturation is dominated by reduction

in τ_r in graphene with increasing photon flux. At low incident optical power density, as $\tau_{TM} \gg \tau_{MG}$ and $\tau_{TM} \gg \tau_{MT}$, the relatively slow de-trapping of carriers builds up larger electron density in the trap states than in the conduction band of the floating MoS₂ gate and thus traps play a major role in photogating and help obtaining the large responsivity. The simulated results follow the experimentally obtained R remarkably well over 11 orders of magnitude of incident optical power density. The minor deviation of the simulated results from the data at smaller wavelength and high optical power density is because the model does not take into account direct absorption in MoS₂. The experimentally obtained R is slightly lower from the model predicted trend line at longer wavelength and is likely due to reduced energy of hot electrons, which affects the injection efficiency from graphene to MoS₂.

In order to estimate the sensitivity of the device, we first extract the root mean squared noise current (N_{RMS}) integrated up to a detection bandwidth of 1 Hz, that is with an averaging time of 0.5 s. The electrical signal-to-noise ratio (SNR) is then obtained as

$$SNR = \frac{I_{ph}}{N_{RMS}} \quad (5)$$

and plotted in Fig. 5c as a function of incident power for different wavelengths. The smallest power incident on the junction during the experiment is 30 fW (@851 nm), and even at such a low power, we obtain an SNR of ~ 10 . Both 532 nm and 633 nm excitations, which directly excite the MoS₂ and WS₂ layers at the junction, produce smaller SNR compared to the larger wavelength excitations. This is attributed to an enhanced noise level due to stronger interaction with SiO₂ traps. The noise equivalent power (NEP) is a figure of merit that is often used to characterize the sensitivity and hence the minimum detectable optical power incident on the photodetector. NEP represents the minimum input power required to obtain unity SNR . The NEP (normalized to 1 Hz)⁶¹ of the detector is then calculated as

$$NEP = \frac{N_{RMS}}{R}|_{SNR=1} \quad (6)$$

Since we only reached $SNR = 10$, from Equation 6, we estimate that the NEP of the photodetector is $< 4 \text{ fW}/\sqrt{Hz}$. The detection limit, as defined by $SNR = 1$ is shown in Fig. 5c by the dashed line. We have shown the performance of another fabricated FLG/2L-WS₂/1L-MoS₂ heterojunction photodetector (D2) in **Supporting Information S1**. D2 exhibits a maximum responsivity of $2.29 \times 10^6 \text{ A/W}$, and $NEP < 10.9 \text{ fW}/\sqrt{Hz}$ at an excitation wavelength of 851 nm.

We benchmark the performance of the photodetector with existing photodetectors using graphene as light absorption medium. We note from the table that the detectors exhibiting high speed of operation suffers from low responsivity, while devices with larger gain show slow response. In this regard, the detector reported in this work not only outperforms any existing graphene-absorption based detector in terms of responsivity by several orders of magnitude, it also simultaneously achieves an extremely low NEP and a fast response.

Table 1: BENCHMARKING TABLE

Device description	Absorbing medium	R (A/W)	NEP (W/ \sqrt{Hz})	Response time (s)
FLG/WS₂/MoS₂ (This work)	Graphene	4.4×10^6	$< 4 \times 10^{-15}$	$< 10^{-2}$
Metal/G/Metal detector ²⁰	Graphene	6.11×10^{-3}	-	25×10^{-12}
Suspended graphene ²³	Graphene	10×10^{-3}	-	-
Graphene with THz antenna ²⁴	Graphene	1.3×10^{-3}	2×10^{-9}	-
G/Ta ₂ O ₅ /G ³⁰	Graphene	$\sim 10^3$	10^{-11}	~ 1
G/MoS ₂ ⁴⁰	Graphene	1.26	7.8×10^{-12}	-
Metal/G/Metal with GQD arrays ⁴⁵	Graphene	8.61	-	~ 100
Plasmonically enhanced graphene ⁶²	Graphene	0.5	-	9×10^{-12}
Biased Graphene ⁶³	Graphene	2.5×10^{-4}	-	-

3 Conclusion

In summary, we have proposed and experimentally demonstrated a new class of highly sensitive photodetector that utilizes graphene as both light absorption medium as well as conduction channel and exploits ultra-fast inter-layer charge transfer to a floating quantum well enabling strong photogating. Graphene being the light absorbing medium, the photodetection principle is appealing for operation over a large wavelength range. The uniqueness of

the device is demonstrated by eliminating the weak sensitivity observed in typical graphene-absorption based detectors. The proposed device achieves significantly superior performance over existing graphene-absorption-based photodetector reports in terms of simultaneously maintaining ultra-high responsivity, high signal to noise ratio at ultra-low incident power, and fast transient response, while reducing system level complexity by automatic flushing of captured photo-carriers when illumination is turned off. The photodetector also holds a key advantage in terms of maintaining room temperature operation, and using low-cost, less hazardous materials. The findings are appealing for highly sensitive broadband photodetection applications.

4 Methods

Device fabrication: The photodetector fabrication process steps are illustrated in Fig. 3a. The device fabrication process starts with mechanical exfoliation of MoS₂ flakes over Si substrate coated with 285 nm SiO₂. 1L-MoS₂ flakes are identified by optical contrast and Raman spectroscopy. We then exfoliate WS₂ flakes on PDMS sheet and identify 2L-WS₂ using optical contrast and confirm with Raman and PL signal. The 2L-WS₂ flake is then transferred on top of the 1L-MoS₂ flake using a micromanipulator under optical microscope. For better adhesion, we heat this stack at 75°C for 2 minutes on a hot plate. For making MoS₂ island, we use electron beam lithography, followed by dry etch using chlorine chemistry. FLG flake is then transferred on the heterostructure using a similar technique discussed above, followed by another heating step. Electrodes for contacting the FLG film are then defined by a second electron beam lithography step, followed by the deposition of Ni (10nm)/ Au (50nm) electrodes by DC sputtering and subsequent lift-off. A third lithography step followed by a final etch step is used to form a regular pattern of the FLG film so that graphene falls only on top of the WS₂/MoS₂ junction area, avoiding any un-gated parallel conduction path.

Acknowledgement

This work was supported in part by a grant under Indian Space Research Organization (ISRO), by the grants under Ramanujan Fellowship, Early Career Award, and Nano Mission from the Department of Science and Technology (DST), and by a grant from MHRD, MeitY and DST Nano Mission through NNetRA.

Supporting Information Available

The following files are available free of charge.

Supporting Information is available on characterization of photodetector D2.

References

- (1) Tan, C. L.; Mohseni, H. Emerging Technologies for High Performance Infrared Detectors. *Nanophotonics* **2018**, *7*, 169–197.
- (2) Martyniuk, P.; Antoszewski, J.; Martyniuk, M.; Faraone, L.; Rogalski, A. New Concepts in Infrared Photodetector Designs. *Applied Physics Reviews* **2014**, *1*, 041102.
- (3) Downs, C.; Vandervelde, T. E. Progress in Infrared Photodetectors Since 2000. *Sensors* **2013**, *13*, 5054–5098.
- (4) Potter, R. F.; Eisenman, W. L. Infrared Photodetectors: A Review of Operational Detectors. *Applied Optics* **1962**, *1*, 567–574.
- (5) Rogalski, A. Recent Progress in Infrared Detector Technologies. *Infrared Physics and Technology* **2011**, *54*, 136–154.
- (6) Craig, A. P.; Thompson, M. D.; Tian, Z. B.; Krishna, S.; Krier, A.; Marshall, A. R. InAsSb-Based nBn Photodetectors: Lattice Mismatched Growth on GaAs and Low-

- Frequency Noise Performance. *Semiconductor Science and Technology* **2015**, *30*, 105011(7pp).
- (7) Gu, Y.; Zhou, L.; Zhang, Y.; Chen, X.; Ma, Y.; Xi, S.; Li, H. Dark Current Suppression in Metamorphic $\text{In}_{0.83}\text{Ga}_{0.17}\text{As}$ Photodetectors with $\text{In}_{0.66}\text{Ga}_{0.34}\text{As}/\text{InAs}$ Superlattice Electron Barrier. *Applied Physics Express* **2015**, *8*, 022202.
 - (8) De Iacovo, A.; Venettacci, C.; Colace, L.; Scopa, L.; Foglia, S. PbS Colloidal Quantum Dot Photodetectors Operating in the Near Infrared. *Scientific Reports* **2016**, *6*, 37913.
 - (9) Cui, D.; Xu, J.; Xu, S. Y.; Paradee, G.; Lewis, B. A.; Gerhold, M. D. Infrared Photodiode Based on Colloidal PbSe Nanocrystal Quantum Dots. *IEEE Transactions on Nanotechnology* **2006**, *5*, 362–367.
 - (10) Hall, D. J.; Buckle, L.; Gordon, N. T.; Giess, J.; Hails, J. E.; Cairns, J. W.; Lawrence, R. M.; Graham, A.; Hall, R. S.; Maltby, C.; Ashley, T. High-Performance Long-Wavelength HgCdTe Infrared Detectors Grown on Silicon Substrates. *Applied Physics Letters* **2004**, *85*, 2113–2115.
 - (11) Lei, W.; Antoszewski, J.; Faraone, L. Progress, Challenges, and Opportunities for HgCdTe Infrared Materials and Detectors. *Applied Physics Reviews* **2015**, *2*, 041303.
 - (12) Mak, K. F.; Ju, L.; Wang, F.; Heinz, T. F. Optical Spectroscopy of Graphene: From the Far Infrared to the Ultraviolet. *Solid State Communications* **2012**, *152*, 1341–1349.
 - (13) Xia, F.; Mueller, T.; Lin, Y. M.; Valdes-Garcia, A.; Avouris, P. Ultrafast Graphene Photodetector. *Nature Nanotechnology* **2009**, *4*, 839–843.
 - (14) Park, J.; Ruiz-vargas, C. Imaging of Photocurrent Generation and Collection in Single-Layer Graphene 2009. *Nano Letters* **2009**, *9*, 1742–1746.
 - (15) Gabor, N. M.; Song, J. C. W.; Ma, Q.; Nair, N. L.; Taychatanapat, T.; Watanabe, K.;

- Taniguchi, T.; Levitov, L. S.; Jarillo-Herrero, P. Hot Carrier-Assisted Intrinsic Photoresponse in Graphene. *Science* **2011**, *334*, 648–653.
- (16) Furchi, M.; Urich, A.; Pospischil, A.; Lilley, G.; Unterrainer, K.; Detz, H.; Klang, P.; Andrews, A. M.; Schrenk, W.; Strasser, G.; Mueller, T. Microcavity-Integrated Graphene Photodetector. *Nano Letters* **2012**, *12*, 2773–2777.
- (17) Nair, R. R.; Blake, P.; Grigorenko, A. N.; Novoselov, K. S.; Booth, T.; Stauber, T.; Peres, N.; Geim, A. K. Fine Structure Constant Defines Visual Transparency of Graphene. *Science* **2008**, *320*, 1308.
- (18) George, P.; Strait, J.; Dawlaty, J.; Shivaraman, S.; Chandrashekhar, M.; Rana, F.; Spencer, M. G. Ultrafast Optical-Pump Terahertz-Probe Spectroscopy of the Carrier Relaxation and Recombination Dynamics in Epitaxial Graphene. *Nano Lett* **2008**, *8*, 4248–4251.
- (19) Rana, F.; George, P. A.; Strait, J. H.; Dawlaty, J.; Shivaraman, S.; Chandrashekhar, M.; Spencer, M. G. Carrier Recombination and Generation Rates for Intravalley and Intervalley Phonon Scattering in Graphene. *Physical Review B* **2009**, *79*, 115447.
- (20) Mueller, T.; Xia, F.; Avouris, P. Graphene Photodetectors for High-Speed Optical Communications. *Nature Photonics* **2010**, *4*, 297–301.
- (21) Yoo, T. J.; Kim, Y. J.; Lee, S. K.; Kang, C. G.; Chang, K. E.; Hwang, H. J.; Revannath, N.; Lee, B. H. Zero-Bias Operation of CVD Graphene Photodetector with Asymmetric Metal Contacts. *ACS Photonics* **2018**, *5*, 365–370.
- (22) Sassi, U.; Parret, R.; Nanot, S.; Bruna, M.; Borini, S.; De Fazio, D.; Zhao, Z.; Lidorikis, E.; Koppens, F. H.; Ferrari, A. C.; Colli, A. Graphene-Based Mid-Infrared Room-Temperature Pyroelectric Bolometers with Ultrahigh Temperature Coefficient of Resistance. *Nature Communications* **2017**, *8*, 1–10.

- (23) Freitag, M.; Low, T.; Avouris, P. Increased Responsivity of Suspended Graphene Photodetectors. *Nano Letters* **2013**, *13*, 1644–1648.
- (24) Spirito, D.; Coquillat, D.; De Bonis, S. L.; Lombardo, A.; Bruna, M.; Ferrari, A. C.; Pellegrini, V.; Tredicucci, A.; Knap, W.; Vitiello, M. S. High Performance Bilayer-Graphene Terahertz Detectors. *Applied Physics Letters* **2014**, *104*, 061111.
- (25) Chen, Z.; Cheng, Z.; Wang, J.; Wan, X.; Shu, C.; Tsang, H. K.; Ho, H. P.; Xu, J. B. High Responsivity, Broadband, and Fast Graphene/Silicon Photodetector in Photoconductor Mode. *Advanced Optical Materials* **2015**, *3*, 1207–1214.
- (26) Chang, K. E.; Yoo, T. J.; Kim, C.; Kim, Y. J.; Lee, S. K.; Kim, S. Y.; Heo, S.; Kwon, M. G.; Lee, B. H. Gate-Controlled Graphene/Silicon Schottky Junction Photodetector. *Small* **2018**, *14*, 1801182.
- (27) Yu, W. J.; Liu, Y.; Zhou, H.; Yin, A.; Li, Z.; Huang, Y.; Duan, X. Highly Efficient Gate-Tunable Photocurrent Generation in Vertical Heterostructures of Layered Materials. *Nature Nanotechnology* **2013**, *8*, 952–958.
- (28) Wan, X. et al. A Self-Powered High-Performance Graphene/Silicon Ultraviolet Photodetector with Ultra-Shallow Junction: Breaking the Limit of Silicon? *npj 2D Materials and Applications* **2017**, *1*, 4.
- (29) Tao, L.; Chen, Z.; Li, X.; Yan, K.; Xu, J.-B. Hybrid Graphene Tunneling Photoconductor with Interface Engineering Towards Fast Photoresponse and High Responsivity. *npj 2D Materials and Applications* **2017**, *1*, 19.
- (30) Liu, C. H.; Chang, Y. C.; Norris, T. B.; Zhong, Z. Graphene Photodetectors with Ultra-Broadband and High Responsivity at Room Temperature. *Nature Nanotechnology* **2014**, *9*, 273–278.

- (31) Konstantatos, G.; Badioli, M.; Gaudreau, L.; Osmond, J.; Bernechea, M.; De Arquer, F. P. G.; Gatti, F.; Koppens, F. H. Hybrid Graphene-Quantum Dot Phototransistors with Ultrahigh Gain. *Nature Nanotechnology* **2012**, *7*, 363–368.
- (32) Roy, K.; Padmanabhan, M.; Goswami, S.; Sai, T. P.; Ramalingam, G.; Raghavan, S.; Ghosh, A. Graphene-MoS₂ Hybrid Structures for Multifunctional Photoresponsive Memory Devices. *Nature nanotechnology* **2013**, *8*, 826–830.
- (33) Yu, W.; Li, S.; Zhang, Y.; Ma, W.; Sun, T.; Yuan, J.; Fu, K.; Bao, Q. Near-Infrared Photodetectors Based on MoTe₂/Graphene Heterostructure with High Responsivity and Flexibility. *Small* **2017**, *13*, 1700268.
- (34) Lan, C.; Li, C.; Wang, S.; He, T.; Zhou, Z.; Wei, D. Highly Responsive and Broadband Photodetectors Based on WS₂-Graphene Van der Waals Epitaxial Heterostructures. *Journal of Materials Chemistry C* **2017**, *5*, 1494–1500.
- (35) Wu, J.-y.; Chun, Y. T.; Li, S.; Zhang, T.; Wang, J. Broadband MoS₂ Field-Effect Phototransistors : Ultrasensitive Visible-Light Photoresponse and Negative Infrared Photoresponse. *Advanced Materials* **2018**,
- (36) Xiong, Y.-f.; Chen, J.-h.; Lu, Y.-q.; Xu, F. Broadband Optical-Fiber-Compatible Photodetector with a Synergetic Photogenerating Mechanism. *Advanced Electronic Materials* **2019**,
- (37) Huo, N.; Gupta, S.; Konstantatos, G. MoS₂–HgTe Quantum Dot Hybrid Photodetectors beyond 2 Å^{−1}m. *Advanced Materials* **2017**, *29*, 1606576.
- (38) Casalino, M.; Russo, R.; Russo, C.; Ciajolo, A.; Gennaro, E. D.; Iodice, M.; Coppola, G. Free-Space Schottky Graphene/Silicon Photodetectors Operating at 2 μm. *ACS Photonics* **2018**, *5*, 4577–4585.

- (39) Zhang, W.; Chuu, C. P.; Huang, J. K.; Chen, C. H.; Tsai, M. L.; Chang, Y. H.; Liang, C. T.; Chen, Y. Z.; Chueh, Y. L.; He, J. H.; Chou, M. Y.; Li, L. J. Ultrahigh-Gain Photodetectors Based on Atomically Thin Graphene-MoS₂ Heterostructures. *Scientific Reports* **2015**, *4*, 3826.
- (40) Vabbina, P.; Choudhary, N.; Chowdhury, A. A.; Sinha, R.; Karabiyik, M.; Das, S.; Choi, W.; Pala, N. Highly Sensitive Wide Bandwidth Photodetector Based on Internal Photoemission in CVD Grown p-Type MoS₂/Graphene Schottky Junction. *ACS Applied Materials and Interfaces* **2015**, *7*, 15206–15213.
- (41) Sun, Z.; Liu, Z.; Li, J.; Tai, G. A.; Lau, S. P.; Yan, F. Infrared Photodetectors Based on CVD-Grown Graphene and PbS Quantum Dots with Ultrahigh Responsivity. *Advanced Materials* **2012**, *24*, 5878–5883.
- (42) Pan, R.; Li, H.; Wang, J.; Jin, X.; Li, Q.; Wu, Z.; Gou, J.; Jiang, Y.; Song, Y. High-Responsivity Photodetectors Based on Formamidinium Lead Halide Perovskite Quantum Dot-Graphene Hybrid. *Particle and Particle Systems Characterization* **2018**, *35*, 1700304.
- (43) Chang, P. H.; Liu, S. Y.; Lan, Y. B.; Tsai, Y. C.; You, X. Q.; Li, C. S.; Huang, K. Y.; Chou, A. S.; Cheng, T. C.; Wang, J. K.; Wu, C. I. Ultrahigh Responsivity and Detectivity Graphene-Perovskite Hybrid Phototransistors by Sequential Vapor Deposition. *Scientific Reports* **2017**, *7*, 46281.
- (44) Li, J.; Yuan, S.; Tang, G.; Li, G.; Liu, D.; Li, J.; Hu, X.; Liu, Y.; Li, J.; Yang, Z.; Liu, S. F.; Liu, Z.; Gao, F.; Yan, F. High-Performance, Self-Powered Photodetectors Based on Perovskite and Graphene. *ACS Applied Materials and Interfaces* **2017**, *9*, 42779–42787.
- (45) Zhang, B. Y.; Liu, T.; Meng, B.; Li, X.; Liang, G.; Hu, X.; Wang, Q. J. Broadband High

- Photoresponse from Pure Monolayer Graphene Photodetector. *Nature Communications* **2013**, *4*, 1811.
- (46) Tan, H.; Xu, W.; Sheng, Y.; Lau, C. S.; Fan, Y.; Chen, Q.; Tweedie, M.; Wang, X.; Zhou, Y.; Warner, J. H. Lateral Graphene-Contacted Vertically Stacked WS₂/MoS₂ Hybrid Photodetectors with Large Gain. *Advanced Materials* **2019**, *1702917*, 1–8.
- (47) Massicotte, M.; Schmidt, P.; Vialla, F.; Schädler, K. G.; Reserbat-Plantey, A.; Watanabe, K.; Taniguchi, T.; Tielrooij, K. J.; Koppens, F. H. Picosecond Photoresponse in Van der Waals Heterostructures. *Nature Nanotechnology* **2016**, *11*, 42–46.
- (48) Hong, X.; Kim, J.; Shi, S.-F.; Zhang, Y.; Jin, C.; Sun, Y.; Tongay, S.; Wu, J.; Zhang, Y.; Wang, F. Ultrafast Charge Transfer in Atomically Thin MoS₂/WS₂ Heterostructures. *Nature Nanotechnology* **2014**, *9*, 682–686.
- (49) Chen, H.; Wen, X.; Zhang, J.; Wu, T.; Gong, Y.; Zhang, X.; Yuan, J.; Yi, C.; Lou, J.; Ajayan, P. M.; Zhuang, W.; Zhang, G.; Zheng, J. Ultrafast Formation of Interlayer Hot Excitons in Atomically Thin MoS₂/WS₂ Heterostructures. *Nature Communications* **2016**, *7*, 12512.
- (50) Hill, M.; F., R. A.; Raja, A.; Chernikov, A.; Roquelet, C.; Heinz, T. F. Exciton Broadening in WS₂ Graphene Heterostructures. *Physical Review B* **2017**, *96*, 205401.
- (51) Nan, H.; Wang, Z.; Wang, W.; Liang, Z.; Lu, Y.; Chen, Q.; He, D.; Tan, P.; Miao, F.; Wang, X.; Wang, J.; Ni, Z. Strong Photoluminescence Enhancement of MoS₂ through Defect Engineering and Oxygen Bonding. *ACS Nano* **2014**, *8*, 5738–5745.
- (52) Ugeda, M. M.; Bradley, A. J.; Shi, S.-F.; da Jornada, F. H.; Zhang, Y.; Qiu, D. Y.; Ruan, W.; Mo, S.-K.; Hussain, Z.; Shen, Z.-X.; Wang, F.; Louie, S. G.; Crommie, M. F. Giant Bandgap Renormalization and Excitonic Effects in a Monolayer Transition Metal Dichalcogenide Semiconductor. *Nature Materials* **2014**, *13*, 1091–1095.

- (53) Gupta, G.; Kallatt, S.; Majumdar, K. Direct Observation of Giant Binding Energy Modulation of Exciton Complexes in Monolayer MoSe₂. *Physical Review B* **2017**, *96*, 081403.
- (54) Koperski, M.; Molas, M. R.; Arora, A.; Nogajewski, K.; Slobodeniuk, A. O.; Faugeras, C.; Potemski, M. Optical Properties of Atomically Thin Transition Metal Dichalcogenides: Observations and Puzzles. *Nanophotonics* **2017**, *6*, 1289–1308.
- (55) Plechinger, G.; Nagler, P.; Arora, A.; Schmidt, R.; Chernikov, A.; del Águila, A. G.; Christianen, P. C.; Bratschitsch, R.; Schüller, C.; Korn, T. Trion Fine Structure and Coupled Spin–Valley Dynamics in Monolayer Tungsten Disulfide. *Nature Communications* **2016**, *7*, 12715.
- (56) Nagler, P.; Ballottin, M. V.; Mitioglu, A. A.; Durnev, M. V.; Taniguchi, T.; Watanabe, K.; Chernikov, A.; Schüller, C.; Glazov, M. M.; Christianen, P. C. M.; Korn, T. Zeeman Splitting and Inverted Polarization of Biexciton Emission in Monolayer WS₂. *Physical Review Letters* **2018**, *121*, 057402.
- (57) Vaclavkova, D.; Wyzula, J.; Nogajewski, K.; Bartos, M.; Slobodeniuk, A. O.; Faugeras, C.; Potemski, M.; Molas, M. R. Singlet and Triplet Trions in WS₂ Monolayer Encapsulated in Hexagonal Boron Nitride. *Nanotechnology* **2018**, *29*, 325705.
- (58) Rana, F. Electron-Hole Generation and Recombination Rates for Coulomb Scattering in Graphene. *Physical Review B* **2007**, *76*, 155431.
- (59) Knobloch, T.; Rzepa, G.; Illarionov, Y. Y.; Walzl, M.; Schanovsky, F.; Stampfer, B.; Furchi, M. M.; Mueller, T.; Grassler, T. A Physical Model for the Hysteresis in MoS₂ Transistors. *IEEE Journal of the Electron Devices Society* **2018**, *6*, 972–978.
- (60) Furchi, M. M.; Polyushkin, D. K.; Pospischil, A.; Mueller, T. Mechanisms of Photoconductivity in Atomically Thin MoS₂. *Nano Letters* **2014**, *14*, 6165–6170.

- (61) Mackowiak, V.; Jens, P.; Ma, Y.; Gorges, A.
https://www.thorlabs.com/images/TabImages/Noise_Equivalent_Power_White_Paper.pdfNEP
 Å§ Noise Equivalent Power. 2007; [https://www.thorlabs.com/images/TabImages/](https://www.thorlabs.com/images/TabImages/Noise_{ }Equivalent_{ }Power_{ }White_{ }Paper.pdf)
[Noise_{ }Equivalent_{ }Power_{ }White_{ }Paper.pdf](https://www.thorlabs.com/images/TabImages/Noise_{ }Equivalent_{ }Power_{ }White_{ }Paper.pdf).
- (62) Ma, P.; Salamin, Y.; Baeuerle, B.; Josten, A.; Heni, W. Plasmonically Enhanced Graphene Photodetector Featuring 100 GBd , High-Responsivity and Compact Size. *ACS Photonics* **2018**,
- (63) Freitag, M.; Low, T.; Xia, F.; Avouris, P. Photoconductivity of Biased Graphene. *Nature Photonics* **2013**, 7, 53–59.

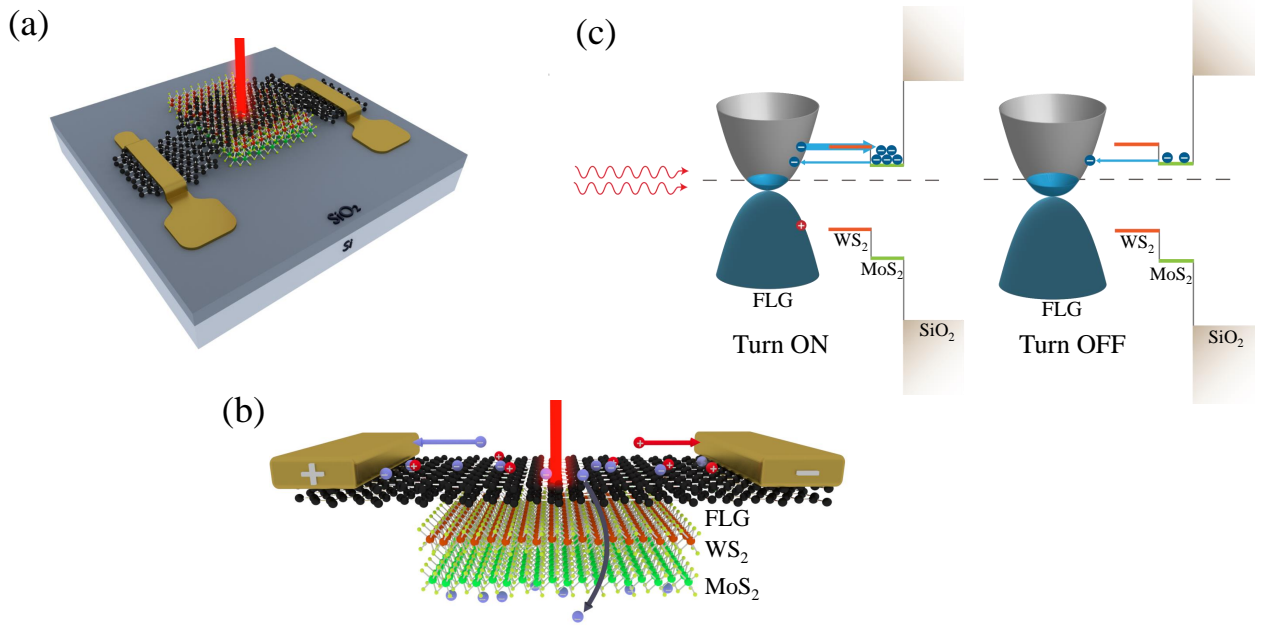


Figure 1: **Proposed photodetector and principle of operation.** (a) Schematic view of the proposed vertical heterojunction device structure. (b) Schematic view of the cross section of the proposed device showing inter-layer transfer of electrons from few layer graphene (FLG) to MoS₂ quantum well under illumination, causing photogating effect. (c) Band diagram along the vertical direction depicting electron exchange between FLG and MoS₂ when illumination is turned ON (left panel), creating a steady state population in MoS₂ causing photogating. When light is turned OFF (right panel), the stored carriers are pushed back to graphene through thin WS₂ tunnel barrier due to built-in field, causing fast turn OFF.

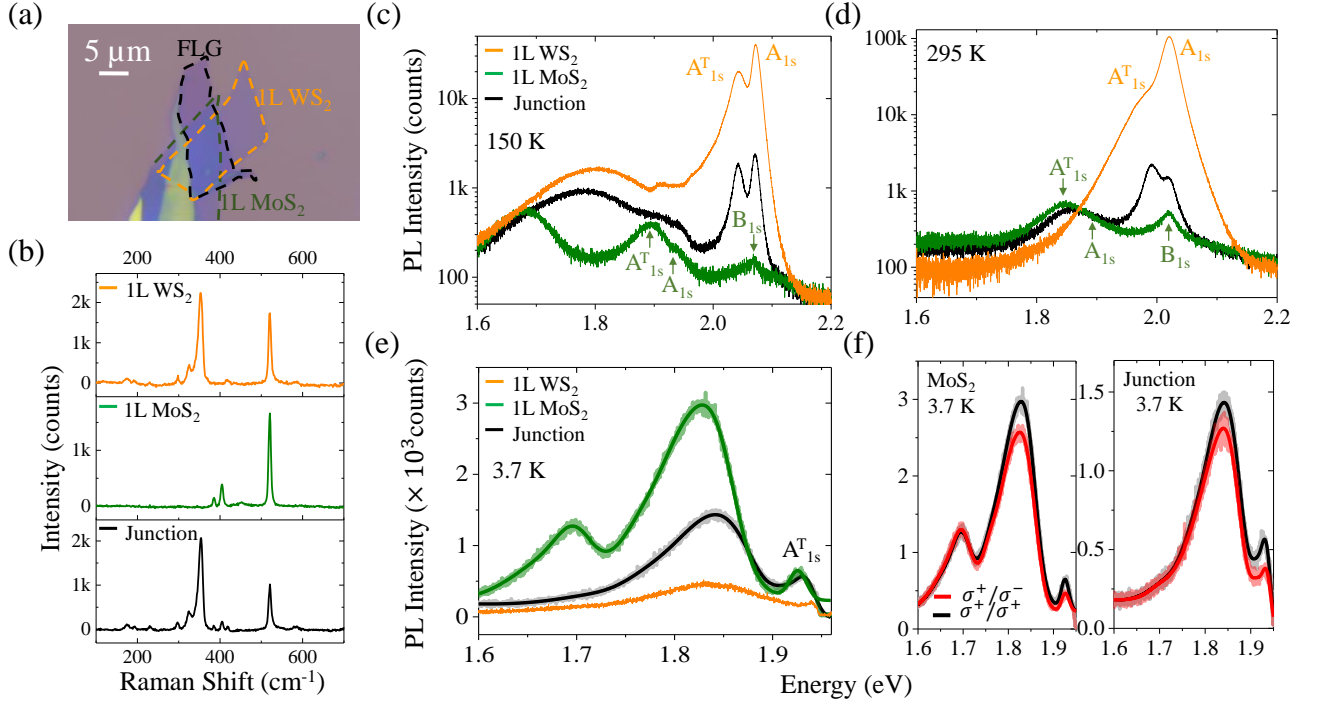


Figure 2: **Evidence of carrier storage in MoS₂ quantum well.** (a) Optical image of a FLG/1L-WS₂/1L-MoS₂ vertical stack, with isolated portions as controls. Perimeter of each layer is shown by dashed lines. (b) Raman spectra of isolated monolayer regions along with the junction (FLG/1L WS₂/1L MoS₂) with 532 nm laser excitation. (c-d) PL intensity (in log scale) of the three regions with 532 nm laser excitation at (c) 150 K and (d) 295 K. The individual exciton and charged exciton (trion) peaks are marked. While WS₂ peaks show strong PL quenching at the junction, the MoS₂ exciton and trion maintain similar luminescence as in the isolated portion, suggesting efficient carrier confinement in MoS₂ quantum well. (e) PL intensity of the three different regions with 633 nm laser excitation at 3.7 K. WS₂ PL is non-existent due to sub-bandgap excitation. MoS₂ trion peak intensity remains unaltered between isolated portion and junction. Strong and broad luminescence below trion peak of MoS₂ indicates existence of sub-bandgap defect states. The exciton peak is truncated by the edge filter. (f) Circular polarization resolved PL on isolated MoS₂ (left panel) and on junction (right panel) using 633 nm excitation, at 3.7 K. The black line indicates σ⁺ excitation and σ⁺ detection, while the red line indicates σ⁺ excitation and σ⁻ detection. Trion valley polarization contrast is found to ~ 25% in both cases.

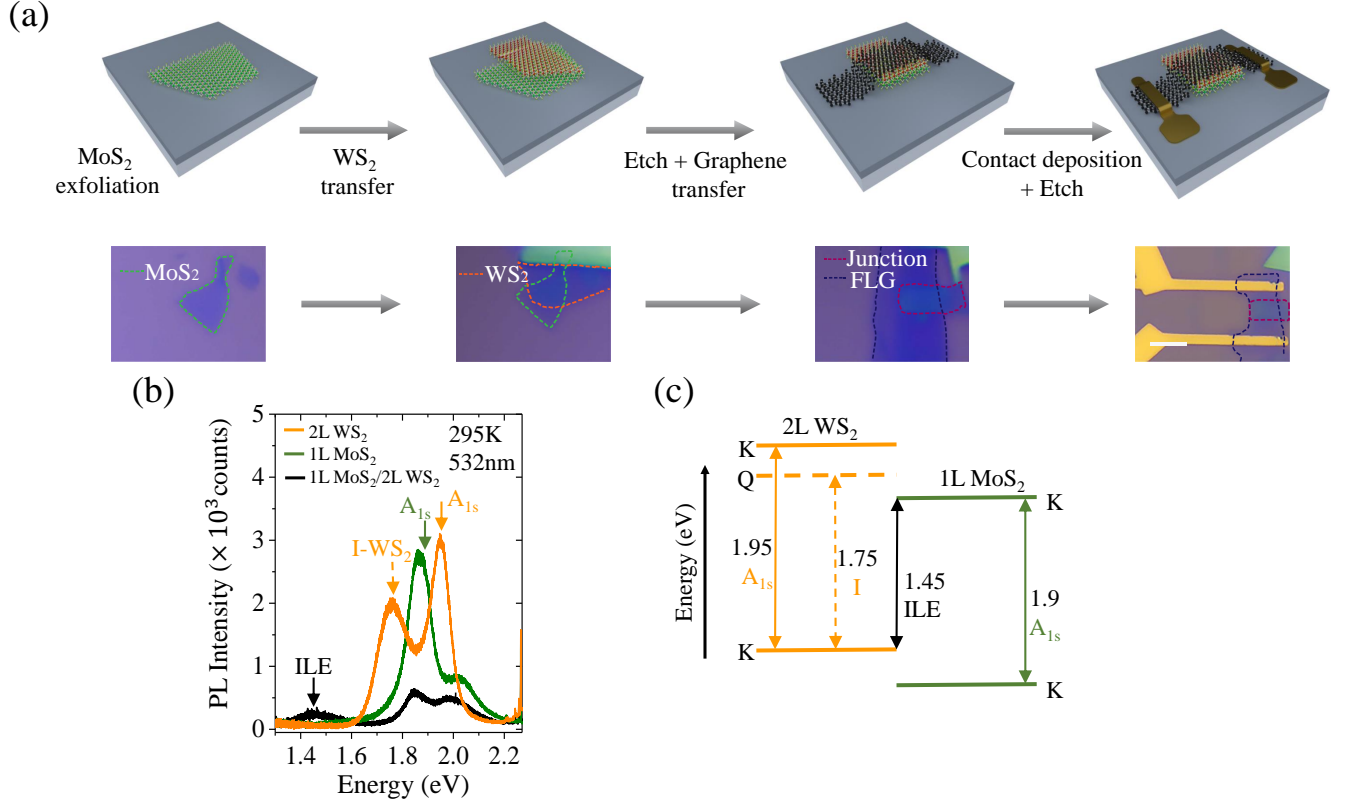


Figure 3: **FLG/2L-WS₂/1L-MoS₂ photodetector fabrication.** (a) Process flow for FLG/2L-WS₂/1L-MoS₂ photodetector fabrication with corresponding optical images at different stages in the bottom row. Scale bar is 5 μm . (b) PL spectra of 2L-WS₂, 1L-MoS₂ and 2L-WS₂/1L-MoS₂ junction. I-WS₂ and ILE indicate the indirect peak of WS₂ and the inter-layer peak between WS₂ and MoS₂, respectively. (c) The band alignment of 2L-WS₂/1L-MoS₂ as obtained from the PL peaks.

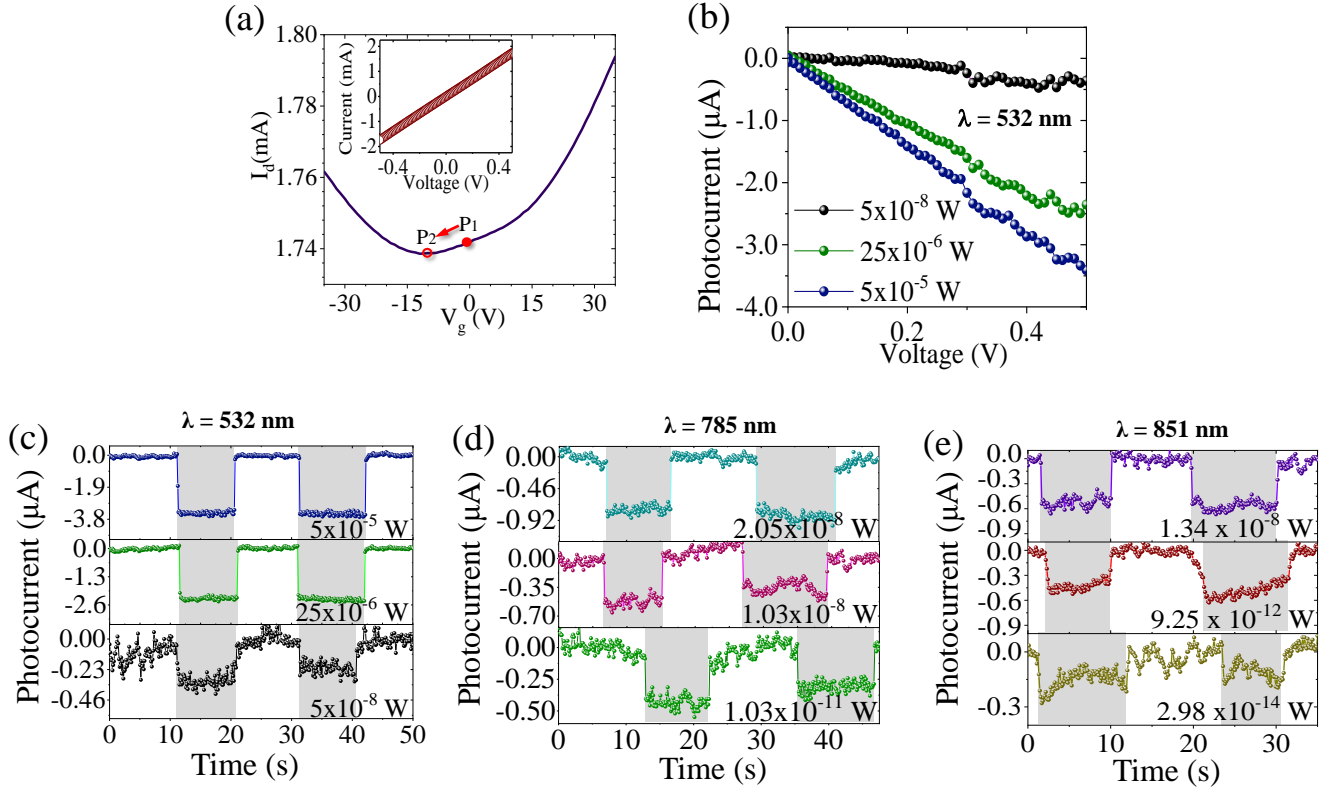


Figure 4: **Characteristics of FLG/2L-WS₂/1L-MoS₂ photodetector.** (a) I_d - V_g plot for FLG under dark condition with $V_d = 0.5$ V. Point P_1 (red, solid circle) shows device operating point under dark condition at zero V_g which shifts to point P_2 (red, open circle) under illumination. Inset: Drain voltage dependant dark current under zero V_g . (b) Photocurrent versus source-drain bias voltage with 532 nm excitation, at three different incident optical powers. (c-e) Transient photoresponse of the proposed graphene photodetector with (c) 532 nm, (d) 785nm and (e) 851 nm excitations at varying optical powers.

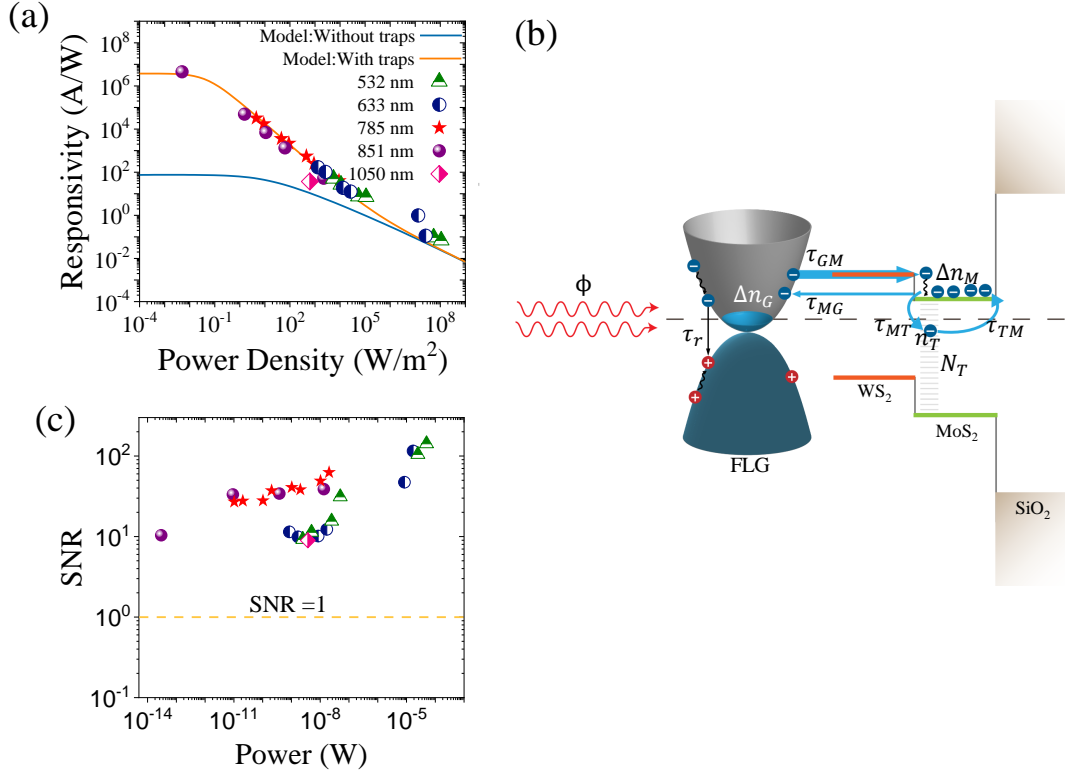


Figure 5: **Performance of FLG/2L-WS₂/1L-MoS₂ photodetector.** (a) Measured (symbols) responsivity versus incident optical power density plot with varying wavelengths. At the minimum power density, the extracted responsivity is 4.4×10^6 A/W. Solid lines in orange and blue represent the model predicted responsivity with and without trap states in MoS₂, respectively. (b) Schematic representation showing different processes captured in the model. (c) Signal-to-noise ratio (*SNR*) of the detector as a function of the actual power falling on the junction. The dashed line indicates the detection limit of the photodetector with *SNR* = 1.

Supporting Information:

Highly Sensitive, Fast Graphene

Photodetector with Responsivity $> 10^6$ A/W

Using Floating Quantum Well Gate

Krishna Murali, Nithin Abraham, Sarthak Das, Sangeeth Kallatt, and Kausik
Majumdar*

*Department of Electrical Communication Engineering,
Indian Institute of Science, Bangalore 560012, India*

E-mail: kausikm@iisc.ac.in

S1. Characterization of photodetector D2

In this section we describe the performance of another few-layer graphene (FLG)/2L-WS₂/1L-MoS₂ vertical heterojunction photodetector (D2). Optical images of the different fabrication steps are shown in Figure S1 (a). The junction area of D2 is 14 μm^2 . The I_d - V_g characteristics of the top few layer graphene shows a negative Dirac voltage, similar to the photodetector D1 presented in the main text. We thus expect a negative photocurrent from D2 as well. The transient response of D2 shows a fast switching for 532, 633 and 851 nm wavelength excitation. As mentioned in the main text, the noise level for 532 and 633 nm wavelength excitation is found to be larger due to direct absorption in MoS₂, which limits the minimum detectable power. However, for 851 nm excitation, like photodetector D1, we are able to detect an extremely low incident power. The responsivity values obtained for device D2 [Figure S1(d)] is comparable with the value obtained for detector D1, with the highest responsivity obtained being 2.29×10^6 A/W. Figure S1(e) shows the calculated signal-to-noise ratio (SNR) value as a function of illumination power falling on the detector. The extracted NEP is $< 10.9 \text{ fW}/\sqrt{\text{Hz}}$ for 851 nm excitation.

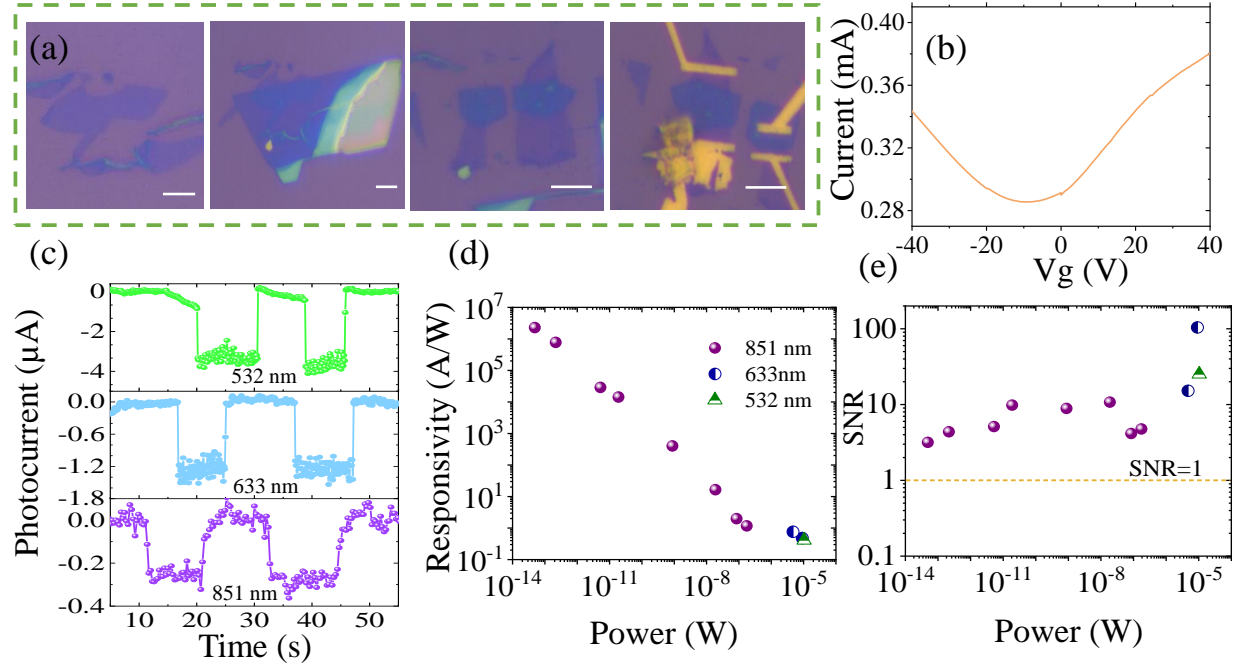


Figure S1: **Characterization of the device 2.** (a) Optical images at the different stages of fabrication of photodetector D2. Scale bar is 5 μm . (b) I_d - V_g characteristics for FLG under dark condition with $V_d = 0.5$ V. (c) Temporal response of D2 at different wavelengths. The optical power incident on the device at 532, 633, and 851 nm are 1.04×10^{-5} , 4.72×10^{-6} , and 1.88×10^{-11} W respectively. (d) Responsivity versus incident optical power at different excitation wavelengths. (e) SNR of the detector as a function of varying optical power.

Graphical TOC Entry

